IEEE Access
Multidisciplinary | Rapid Review | Open Access Journal

Received May 7, 2019, accepted May 25, 2019, date of publication May 31, 2019, date of current version June 18, 2019.

Digital Object Identifier 10.1109/ACCESS.2019.2920146

An Averaged Intensity Difference Detection Algorithm for Identification of Human Gingival Sulcus in Optical Coherence Tomography Images

NARESH KUMAR RAVICHANDRAN[1], HOSEONG CHO[1], JAEYUL LEE[1], SANGYEOB HAN[1], RUCHIRE ERANGA WIJESINGHE[2], PILUN KIM[3], JAE-WON SONG[1], MANSIK JEON[1], AND JEEHYUN KIM[1]

[1]School of Electronics Engineering, College of IT Engineering, Kyungpook National University, Daegu 41566, South Korea
[2]Department of Biomedical Engineering, College of Engineering, Kyungil University, Gyeongsangbuk-do 38428, South Korea
[3]Institute of Biomedical Engineering, Kyungpook National University, Daegu 41944, South Korea

Corresponding author: Mansik Jeon (msjeon@knu.ac.kr)

This work was supported in part by the Bio and Medical Technology Development Program of the NRF funded by the Korean Government, MSIP, under Grant 2017M3A9E2065282, in part by the National Research Foundation of Korea (NRF) grants funded by the Korean Government, MSIT, under Grant 2018R1A5A1025137, in part by the BK21 Plus Project funded by the Ministry of Education, South Korea, under Grant 21A20131600011, and in part by the Basic Science Research Program through the National Research Foundation of Korea (NRF) funded by the Ministry of Education under Grant 2018R1D1A1B07043340.

ABSTRACT In the past decade, there has been an increase in the development of sensitive, high-resolution, non-invasive diagnostic methods for periodontic diseases. Optical coherence tomography (OCT) has attracted considerable attention in clinical settings. In this paper, a reliable, robust algorithm for the detection of gingival sulcus in 2D OCT cross-sectional images is proposed. Previously, the measurement of gingival sulcus in OCT images has been performed by manual identification using two-dimensional (2D) cross-sectional images. The automated detection of gingival sulcus continuity in 2D OCT images may help medical practitioners to assess important features of gingival tissues. The Sobel and canny operators have mainly been used for boundary and edge detection in OCT images. However, these algorithms are highly sensitive to noise and speckle in OCT images. To overcome these limitations, we propose an algorithm for the quantitative depth measurement of the human gingival sulcus, based on averaged intensity difference. In this paper, we utilized two commercially-available swept-source OCT systems operating at center wavelengths of 1310 and 1060 nm to image gingival sulcus of human samples in vivo. The images were processed using three algorithms: canny, Sobel, and averaged intensity difference.

INDEX TERMS Biomedical optical imaging, detection algorithms, optical coherence tomography.

I. INTRODUCTION

Gingiva is the soft tissue that is present around the teeth. The gingival sulcus is the naturally-occurring space between the teeth and gingival tissues. The depth of the gingival sulcus is determined by the connective tissues and by the free gingival margin. Food residue and plaque formation in the gingival sulcus results in a widening or increase in the depth of the gingival sulcus, resulting in abnormally loosened teeth and subsequent periodontal diseases. Periodontal disease, which can take years to develop, is now believed to be associated with health problems such as cardiovascular disease [1] and diabetes [2]. In a recent study, it had been shown that in the United States between 2009 and 2010, approximately 47% of the population aged 30 years and older are affected by some forms of periodontitis [3].

In clinical practice probing of periodontal pockets is the most commonly-used method for quantifying periodontal status, based on attachment loss and the depth of the gingival sulcus. Probing is a minimally invasive procedure, yet it can induce or increase separation between gingival tissue and the tooth surface [4]. The same procedure is also used for

The associate editor coordinating the review of this manuscript and approving it for publication was Vishal Srivastava.

assessing periodontal disease and deciding upon treatment procedures [5], [6]. Probing analysis only presents a retrospective perspective of the attachment. The procedure is also susceptible to variations due to manual pressure, probing angle, instrument caliber, and the condition of tissues. Dental radiographs, however, provide non-invasive images which provide information about root length, presence or absence of periapical lesions, dental calculus, root proximity, and remaining alveolar bone [7]. Due to the limited resolution of dental radiography, it is difficult to measure the gingival sulcus depth using two-dimensional (2D) dental radiograph images [8]. The use of dental radiography also involves exposure to ionizing radiation, and provides no information about the state of the soft tissues. As an alternative, cone-beam computed tomography is routinely used in clinical practice for the imaging of soft and hard tissues, especially for oral pathology [8]. However, it has low spatial resolution and the exposes the patient to ionizing radiation. When it comes to experimental and research studies, techniques like micro-CT [9] and histology [10] have predominantly been used for studying gingival tissues. These techniques involve sectioning as necessary for histology, or high exposure to ionizing radiation like in case of dental radiography or in micro-CT imaging as they use X-ray source.

Among the non-invasive imaging techniques, optical coherence tomography (OCT) has been recognized for its versatility in applications to biomedical imaging. OCT uses near-infrared laser light as a light source, and utilizes low-coherence interferometry techniques to produce high-resolution, non-invasive 2D cross-sectional images in real time. Owing to its high-resolution imaging capabilities, OCT is being utilized for the study of microstructures, borders, thickness, and the anatomy of dental tissues such as enamel, enamel cracks, dentin, plaque, periodontal, periodontal tissue structure monitoring, and orthodontic microimplants [11]–[19]. OCT has also been applied to the measurement of gingival sulcus in small animal models, pigs and humans [20]–[23]. Recent studies have focused on improving the accuracy of measuring pocket depth [24]. Polarization-sensitive OCT (PS-OCT) [25] and OCT angiography (OCTA) [26] have been shown to be effective in visualizing gingival microvasculature with high resolution. Previous research has shown the usefulness of Sobel and canny edge operators for edge detection in OCT image post-processing. These algorithms have also been used for image layer segmentation and the detection of individual layers in OCT [27], [28]. However, these operators are highly sensitive to noise and speckle variations in OCT images.

In this study, we propose a detection algorithm based on averaged intensity difference in the OCT images. To demonstrate the effectiveness of the algorithm we imaged the gingival sulcus of human samples *in vivo* using two commercially available swept-source OCT (SS-OCT) systems, which were centered at 1310nm and 1060nm. The 2D cross-sectional OCT images were analyzed in post-processing for the identification of gingival sulcus. The images were processed using three detection algorithms: canny, Sobel and averaged intensity difference.

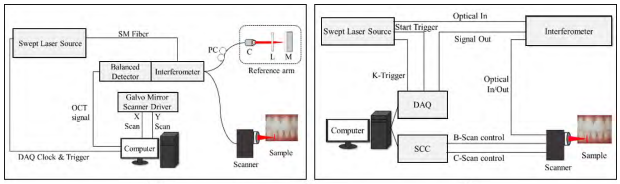

Parameters	Thorlabs OCS1310V1	Santec IVS-1000
Source type	Swept-source laser	Swept-source laser
Center wavelength	1310 nm ± 15 nm	1060 nm ± 15 nm
Spectral bandwidth	97 nm	100 nm
Axial scan rate	100 kHz	100 kHz
Sensitivity	105 dB	101 dB
Transverse resolution (In air)	25 µm	20 µm
Axial resolution (In air)	18 µm	16 µm
Optical Power on sample	8 mW	10 mW

(C)

FIGURE 1. Schematic diagram of the 1310 nm and 1060 nm SS-OCT system along with specifications. (A) Schematic diagram representing the SS-OCT system setup of Thorlabs OCS1310V1, which has a center wavelength of 1310nm. (B) Schematic diagram representing the SS-OCT system setup of Santec IVS-1000, which has a center wavelength of 1060nm. (C) Tabulated comparison with parameters of the Thorlabs OCS1310V1 and Santec IVS-1000 SS-OCT systems.

II. MATERIALS AND METHODS

A. SAMPLE ARMAMENTARIUM

In vivo imaging of human samples was performed on eight individual healthy volunteers aged between 20 and 30 years. During imaging of the gingival sulcus, a lip retractor and a bench-top head holder were utilized to keep the teeth position stable. The lower central incisors of each individual were imaged for identifying the gingival sulcus. All of the human experiments were performed in accordance with the guidelines of the Institutional Animal and Human Care and Use Committee of Kyungpook National University (No. 2017-0145-1). The amount of coherently backscattered light in highly turbid media decays exponentially with depth, resulting in axial compression of the image. For this reason, the OCT axial depth scale should be calculated by dividing the refractive index of the relevant tissue regions, such as 1.3 for oral mucosa, 1.6 for enamel and gum, 1.5 for dentin and 1.4 for gingival sulcus, to obtain true physical dimensions. The refractive index of gingival tissue used for this study was 1.41 ± 0.06 [20].

B. OCT SYSTEM CONFIGURATION

In this study, we used two commercially available SS-OCT systems for imaging the gingival tissues: a Thorlabs OCS1310V1 (Thorlabs. Inc, Newton, New Jersey, United States), and a Santec IVS-1000 (Santec. Inc, Aichi, Japan). A schematic of the OCT system setup is shown in Figure 1 (A) and (B). A brief detail of both OCT system specifications is shown in Figure 1 (C).

1) 1310 NM SS-OCT SYSTEM SETUP

The Thorlabs OCS1310V1 OCT system is powered by a micro-electro-mechanical system (MEMS) tunable vertical cavity surface emitting laser (VCSEL) swept laser source which was centered at 1310 nm. The sweeping rate was 100 kHz and the full width half maximum (FWHM) spectral bandwidth of the source was 97nm. A small portion of the output beam from the VCSEL laser cavity module was projected into a Mach–Zehnder interferometer (MZI) clock module to achieve real-time optical clocking, using which OCT spectral fringes can be evenly sampled in wavenumbers with the referenced MZI signals, eliminating the necessity of postprocessing for fringe resampling. The remaining output beam of the source laser was coupled into the main OCT interferometer, which was connected to a circulator. The output arm of the circulator (within the interferometer) was connected to an optical coupler in a 50:50 ratio. The coupler outlets were connected to a sample arm and reference arm setup. The back-reflected optical signals interfere in the optical coupler and the output end of the coupler and the final output from the circulator arm were connected to the positive and negative terminals of the dual balanced photodetector. The sample arm setup consisted of a 2D galvanometer scanner and an objective scan lens of N.A. = 0.055. The reference arm setup comprised a collimator, a lens, and a highly reflective mirror. The interference signal from the dual balanced photodetector was linearly sampled by a 12 bit, 500 MS/s data acquisition card. The depth-dependent reflectivity profile (A-line) was produced by fast Fourier transformation of the sampled fringe signals, and by using the galvanometer scanner two-dimensional cross-sectional OCT image was generated in real time. The sensitivity of the OCT system was 105dB. The axial and transverse resolutions of the system in air was 18 μm and 25 μm respectively.

2) 1060 NM SS-OCT SYSTEM

The Santec IVS-1000 OCT system was powered by a VCSEL tunable type swept source laser which was centered at 1060nm. The spectral bandwidth full width half maximum (FWHM) of the swept source laser was 100nm. The axial scan rate of the swept laser was 100 kHz. The output beam from the laser source was connected to Mach–Zehnder interferometer (MZI). The MZI setup consisted of an optical coupler of 50:50 ratio. The two output ends of the couplers were connected to a reference arm and a sample arm. The reference beam was connected to a polarization controller followed by an optical circulator. The first output end of the circulator was connected to a collimator, a focusing lens and a highly reflective mirror. The back-reflected beam from the mirror was obtained from the final output arm of the circulator. The sample beam from the beam splitter was connected to a polarization controller followed by an optical coupler. The first output end of the circulator was connected to a collimating lens through a fiber connector. The collimated beam was then aligned onto two-axis galvanometer mirror scanners followed by an objective lens which focused the sampling beam on to the sample surface. The back-reflected sample arm beam was collected in the final output arm of the optical circulator connected in the sample arm. The path length-matched back-reflected sample arm and reference arm optical beams were then coupled for interference using an optical coupler. The final interfered signals from the outputs of the coupler arms were then connected to a dual-balanced photodetector. The final signal was linearly sampled using a high-speed data acquisition 12 bit, 100 MHz board. The depth-dependent reflectivity profile (A-line) was produced by fast Fourier transformation of the sampled fringe signals, and a synchronized control circuit (SCC) two-axis galvanometer mirror scanners were controlled for generating continuous two-dimensional cross-sectional OCT images in real time. The sensitivity of the OCT system was 101dB. The axial and transverse resolutions of the system in air was 16μm and 20μm respectively. We used a scan range of 6mm for acquiring 2D OCT images. The scan range was maintained in both SS-OCT systems for all *in vivo* experiments.

III. DETECTION ALGORITHMS FOR IDENTIFICATION OF HUMAN GINGIVAL SULCUS

A. CANNY AND SOBEL OPERATORS FOR DETECTION OF THE GINGIVAL SULCUS

For detection of gingival sulcus using the Sobel operator, we used two 3×3 masks. One estimated the gradient in the x-direction (axial/ depth) and the other estimated the gradient in the y-direction (transverse/lateral). The algorithm calculates the gradient of the image intensity at each point in the image. The algorithm then calculates the direction in which to increase the image intensity at each point from bright to dark. This identifies image areas with darker or brighter intensity contrast, representing the edges in the final image.

In the case of the canny detection algorithm, the image is initially blurred to reduce noise. The canny operator then takes the directional gradient of all points in the entire image, in the x and y directions, and marks the gradients with larger magnitude as edges. The magnitude of the gradient of each pixel is checked as to whether it is greater than the next pixel in either its positive or negative direction perpendicular to the gradient. If the pixel is not greater than either of the magnitudes it is suppressed. Finally, the edges are highlighted with both a high and low threshold. In the final operation, the edges are determined by suppressing the edges that are not connected to a stronger edge with high gradient magnitude.

B. PROPOSED AVERAGED INTENSITY DIFFERENCE ALGORITHM FOR DETECTION OF THE GINGIVAL SULCUS

In our proposed algorithm, edge detection is carried out by calculating the averaged intensity difference at every pixel,

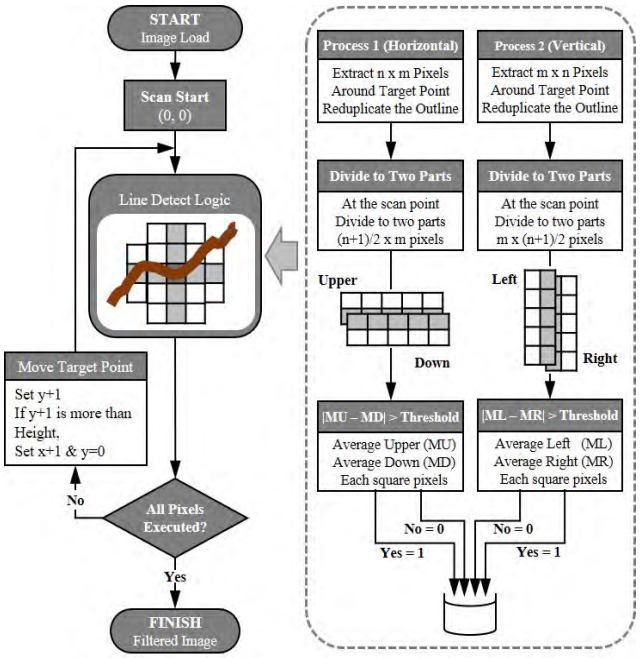

FIGURE 2. Flow diagram representation illustrating the steps involved in averaged intensity difference edge detection algorithm.

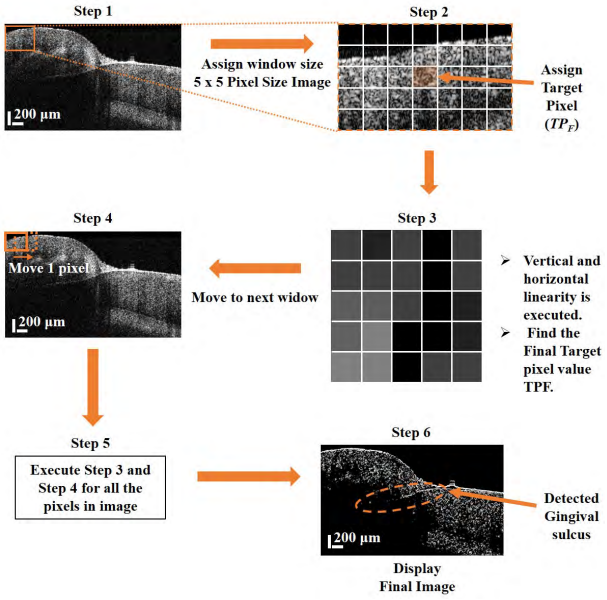

FIGURE 3. Detailed step by step process involved in averaged intensity difference edge detection algorithm with an example of OCT image.

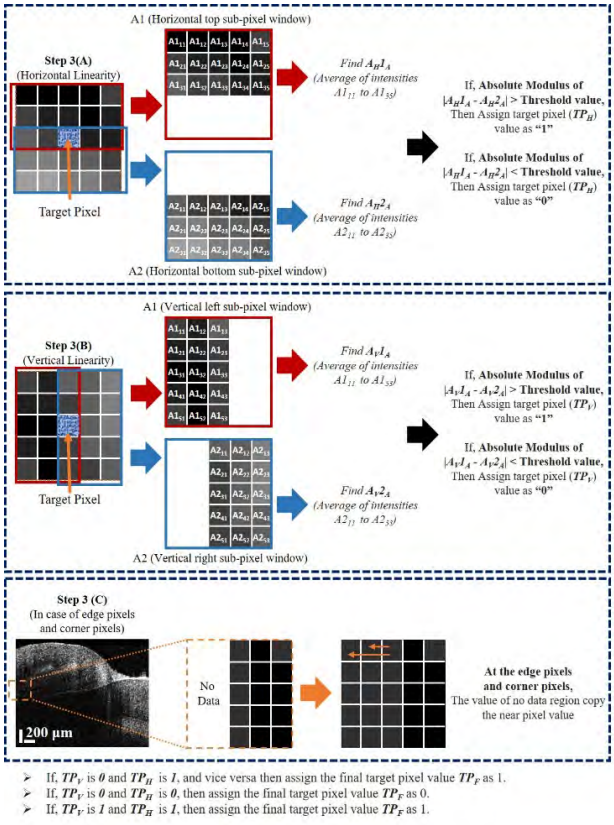

FIGURE 4. Detailed explanation of vertical and horizontal linearity process.

in order to identify the boundaries in the image. The algorithm was written in Matlab. The flow diagram illustrating the steps involved in the averaged intensity difference detection algorithm is shown in Figure 2.

The workflow begins with loading the OCT image, followed by scanning the image pixels; the line detection algorithm. The line detection algorithm comprises two processes, vertical and horizontal linearity. In the horizontal detection process, a pixel window size of $n \times m$ is selected, and the center pixel is assigned as the target pixel. Then the pixel window is split into two sub-pixel windows, the horizontal top, and the horizontal bottom, with the center row containing the target pixel in both the sub-windows. The intensity of all of the pixels within the horizontal top sub-pixel window is summed and averaged, as are those in the horizontal bottom sub-window. The difference between the average intensities of the horizontal top and the horizontal bottom is calculated, and absolute modulus of the value is estimated. This absolute modulus value is compared with a predefined threshold value. If it is higher, the target pixel is assigned a value of 1. If it is less than the threshold it is assigned a value of 0. The target pixel is then shifted by one pixel, moving the initial full pixel window of size $n \times m$ by one pixel in the horizontal direction. The target pixel value is re-calculated as previously described.

The same procedure is executed in the vertical direction These two processes are executed for the entire image, thereby assigning a value of either 1 or 0 to each pixel in the OCT image. If the final processed OCT image is does not meet the requirements for edge detection then the predefined threshold value is increased or decreased as needed.

Figures 3 and 4 shows the details of the averaged intensity difference edge detection algorithm, using an example of an OCT image. The averaged intensity difference detection algorithm can be classified into six individual steps. Step 1 is

loading the OCT image and assigning a fixed pixel window size of $n \times m$ and $m \times n$ horizontal linearity and vertical linearity processes, respectively. The values of m and n are chosen according to the sensitivity requirements of the edge detection of the OCT image. In step 2, the center pixel is assigned as the target pixel in its respective horizontal and vertical pixel windows (Figure 3).

Step 3 is the execution of the horizontal and vertical linearity process. This step can be further classified as steps 3 (A), (B), and (C) (Figure 4). In this step, after assigning the pixel window size, each horizontal and vertical linearity pixel window is sub-divided into sub-pixel windows in such a way that the target pixel (center pixel) is present in both sub-pixel windows. In step 3 (A) the row containing the target pixel is present in both the horizontal top and horizontal bottom sub-pixel windows. Then all of the intensities of the pixels in the horizontal top sub-pixel window are summed and averaged and assigned as $A_H 1_A$. Similarly, all the intensities of pixels in horizontal bottom sub-pixel window are summed and averaged as $A_H 2_A$. If the absolute modulus of the difference between $A_H 1_A$ and $A_H 2_A$ is higher than the predefined threshold value, the target pixel (TP_H) is assigned the value 1, while if the absolute modulus of the difference between $A_H 1_A$ and $A_H 2_A$ is less than the predefined threshold value, the target pixel (TP_H) is assigned the value 0. As in step 3 (A), in step 3 (B) for the vertical linearity pixel window, the column containing the target pixel is present in both the vertical left and vertical right sub-pixel windows. All of the intensities of the pixels in the vertical left sub-pixel window are summed and averaged and assigned as $A_V 1_A$. All of the intensities of the pixels in the vertical right sub-pixel window are summed and averaged as $A_V 2_A$. If the absolute modulus of the difference between $A_V 1_A$ and $A_V 2_A$ is higher than the predefined threshold value, then the target pixel (TP_V) is assigned the value 1, if the absolute modulus of the difference between $A_V 1_A$ and $A_V 2_A$ is less than the predefined threshold value, then the target pixel (TP_V) is assigned the value 0. Finally, the values of TP_H and TP_V are compared. If TP_V is 0 and TP_H is 1, or vice versa then the final target pixel (TP_F) is assigned a value of 1. If both TP_H and TP_V are 0, then the final target pixel (TP_F) is assigned to be 1., If both TP_H and TP_V are 1, then the final target pixel (TP_F) is 1. In the case of edge and corner pixels, as shown in step 3 (C) of Figure 4, when the target pixel (center pixel) is in the first column or row, we copy the data values of pixels in the target columns or rows and shift and paste in vertical left or vertical right, or in the horizontal top or in the horizontal bottom as required (Figure 4C).

In step 4, the target pixel is shifted by one pixel horizontally. This is achieved by shifting the fixed pixel window size by one pixel to the right. Step 5 is a repetition of step 3 and 4 until all of the pixels in the 2D OCT image have been assigned as a target pixel and are assigned a value of either 0 or 1. When executing step 4, if the moving of the fixed pixel window reaches the corner or the edge of any side of the OCT image then the pixel window is moved down and then moved to the left or right as required. Step 6 is the final projection of the edge-detected 2D OCT image by the averaged intensity difference algorithm. If the final image is not as expected, and if the gingival sulcus is not sufficiently visible, then the threshold value which is used in the algorithm is changed as needed to achieve an identifiable gingival sulcus in the final processed OCT image.

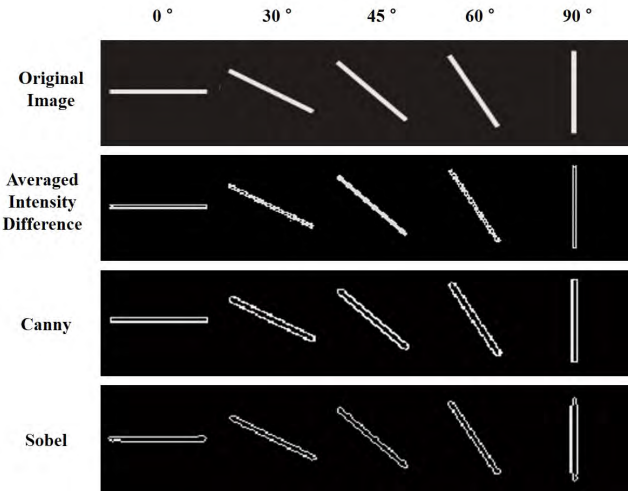

FIGURE 5. Comparative analysis of Sobel, canny and averaged intensity difference edge detection algorithms using phantom samples. Five phantom samples (solid lines) with a black background induced with a tilt angle of 0°, 30°, 45°, 60°, and 90° created using Microsoft office toolkit, which was then saved as a JPEG image. Sobel, canny and averaged intensity difference edge detection algorithms were used for detecting the edges of all five samples.

IV. RESULTS AND DISCUSSION

A. COMPARISON OF EDGE DETECTION ALGORITHMS USING PHANTOM

To evaluate the efficiency of the proposed algorithm for edge detection, and to compare it with the canny and Sobel edge detection algorithms, we created a phantom sample. The phantom was created using the Microsoft office toolkit in form of five solid lines of continuous intensity (white) on a black background. It was then saved as a JPEG image with dimensions 32.25mm (height) by 165.6mm (width). The length of each solid line in the phantom 31.5mm and width 0.508mm. The crated five solid lines had angles of 0°, 30°, 45°, 60°, and 90°, respectively. The length, width, and angles of the solid lines were selected as necessary to evaluate the efficiencies of the detection algorithms.

Figure 5 shows the original phantom image with the final edge detected images as executed by the canny, Sobel and averaged intensity different algorithms. Figure 5 shows that all three algorithms detect the edges of the solid lines in the phantom at all angles. Upon closer inspection, however, it is apparent that as the tilt angle of the solid lines increases the canny and Sobel edge detection algorithms show an increase in the width of the solid lines detected. It can also be seen that the edges detected by these algorithms are not smooth

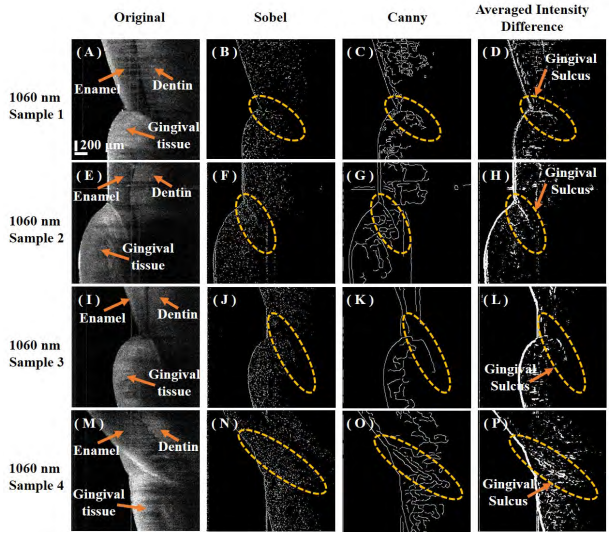

FIGURE 6. Sobel, canny, and averaged intensity difference edge detection algorithm for gingival sulcus identification in 1060 nm SS-OCT images. (A), (E), (I), and (M) are the original 2D OCT images of human gingival sulcus, obtained using 1310 nm SS-OCT system. (B), (F), (J), and (N) is the edge detected OCT images using a Sobel edge detection algorithm. (C), (G), (K), and (O) are the edge detected OCT images using canny edge detection algorithm. (D), (H), (L), and (P) are the edge detected OCT images using the proposed averaged intensity difference edge detection algorithm. The identified gingival sulcus is shown within the yellow dotted ellipse in the edge detected images.

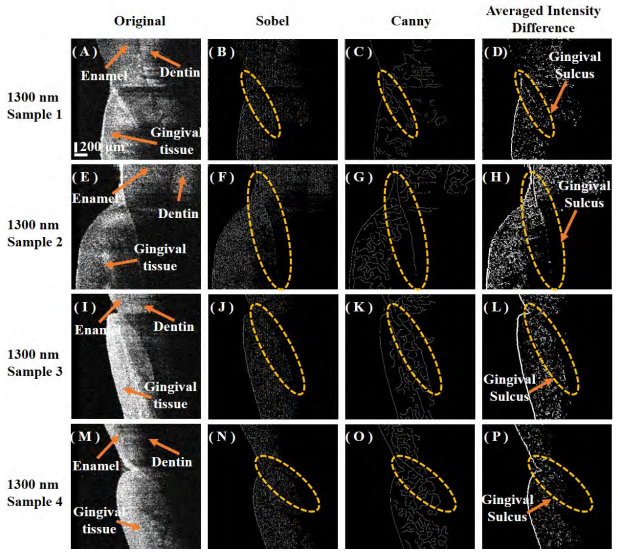

FIGURE 7. Sobel, canny, and averaged intensity difference edge detection algorithm for gingival sulcus identification in 1310 nm SS-OCT images. (A), (E), (I), and (M) are the original 2D OCT images of human gingival sulcus, obtained using 1310 nm SS-OCT system. (B), (F), (J), and (N) is the edge detected OCT images using a Sobel edge detection algorithm. (C), (G), (K), and (O) are the edge detected OCT images using canny edge detection algorithm. (D), (H), (L), and (P) are the edge detected OCT images using the proposed averaged intensity difference edge detection algorithm. The identified gingival sulcus is shown within the yellow dotted ellipse in the edge detected images.

in the solid lines tilted at 30°, 45°, and 60°. In the case of the proposed averaged intensity difference edge detection algorithm, the width of the edge detected solid lines in all tilt angels is constant, with a very small or negligible increase when compared to a horizontal solid line (0° tilt) or vertical solid line (90° tilt). Additionally, the edges detected in tilted solid lines have smoother edges when compared with those detected by the two canny and Sobel algorithms.

B. DETECTION IDENTIFICATION OF HUMAN GINGIVAL SULCUS USING THE PROPOSED ALGORITHM

Eight healthy patients were separated into two groups of four. The first group of patients was imaged using the 1310nm SS-OCT system and the rest were imaged using the 1060nm SS-OCT system. To avoid involuntary movements by the patients, they were seated in an upright position with their chins rested on a bench-top head holder, and a lip retractor was positioned to keep their mouths open during the imaging process. All OCT imaging was done on the patients' lower central incisors, and the scanning position was aligned such that the region of interest was focused on the boundary between tooth and gingival tissues. The sample arm focusing was set to few micrometers below the gingival tissue where the gingival sulcus is present. Multiple 2D OCT images were acquired for each patient along the region of interest, so that the best fitting OCT image could be selected, where the gingival sulcus could be seen in the OCT image.

Figure 6 shows the 2D cross-sectional OCT images of samples that were acquired with the 1060nm SS-OCT system. In Figure 6, images (A), (E), (I), and (M) are the original 2D cross-sectional OCT images. The enamel, dentin and gingival tissues are marked with solid arrows in the OCT images. Images (B), (C), and (D) are the edge-detected final images obtained using the Sobel, canny and averaged intensity difference algorithms respectively. Images (F), (G), and (H) are the final processed images of sample (E), images (J), (K), and (L) are the final processed images of sample (I), and images (N), (O), and (P) are the final processed images of sample (M). In all edge-detection processed images, the estimated position of the gingival sulcus is shown with a yellow dotted ellipse. From the processed images it can be observed that images processed with the Sobel algorithms show the least identifiable gingival sulcus. In the canny edge detected images, the gingival sulcus is fairly visible, but the detected gingival sulcus lacks continuity, and the structure looks irregular (Image C). In the averaged intensity difference edge detected images, the continuity and intensity of the gingival sulcus are apparent.

Figure 7 shows the 2D cross-sectional OCT images of samples that were acquired using the SS-OCT system with a center wavelength of 1310nm. In Figure 7, images (A), (E), (I), and (M) are the original 2D cross-sectional OCT images. When compared with the 1060nm OCT images, the images acquired at 1310nm show more prominent depth resolution of structures. The internal structures of the samples, such as enamel, dentin, and gingival tissues, are marked with solid arrows in the OCT images. Images (B), (C), and (D) are the edge-detected final images obtained using the Sobel, canny

TABLE 1. Pixel window size, the total time taken for processing, and intensity threshold values used for canny, Sobel, and averaged intensity difference edge detection algorithms executed for 1060 nm SS-OCT 2D images.

For Images taken using 1060 nm SS-OCT			
Total time taken for processing (seconds)			
Sobel	Canny	Averaged Intensity Difference	
		Pixel window Size	-
5 ± 1	18 ± 1	(m × n = 7 x 7)	160 ± 10
		(m × n = 9 x 7)	200 ± 15
	Sobel	Canny	Averaged Intensity Difference
Intensity Threshold (A.U.)	31 ± 5	0.21 ± 0.05	0.088 ± 0.015

TABLE 2. Pixel window size, the total time taken for processing, and intensity threshold values used for canny, Sobel, and averaged intensity difference edge detection algorithms executed for 1310 nm SS-OCT 2D images.

For Images taken using 1310 nm SS-OCT			
Total time taken for processing (seconds)			
Sobel	Canny	Averaged Intensity Difference	
		Pixel window Size	-
8 ± 1	62 ± 1	(m × n = 7 x 7)	1050 ± 15
		(m × n = 9 x 7)	1280 ± 25
	Sobel	Canny	Averaged Intensity Difference
Intensity Threshold (A.U.)	25 ± 5	0.25 ± 0.05	0.135 ± 0.035

and averaged intensity difference algorithms respectively. Images (F), (G), and (H) are the final processed images of sample (E); images (J), (K), and (L) are the final processed images of sample (I); and images (N), (O), and (P) are the final processed images of sample (M). In all of the edge-detected images, the estimated position of the gingival sulcus is shown with a yellow dotted ellipse. In the case of the Sobel edge-detected images the identification of the gingival sulcus is much more difficult and the continuity is lower in comparison to the other detection algorithms. In the canny edge-detected images the continuity of the gingival sulcus is consistent, as seen in Figure 6, images (C), (G), (K), and (O). The irregularity in the shape of the identifiable gingival sulcus can lead to the wrong identification of the surrounding gingival tissues for the gingival sulcus. In the averaged intensity difference edge-detected images, the continuity and intensity of the gingival sulcus are consistent. The proposed algorithm highlights the intensity of the gingival sulcus without changing the detection of its shape or thickness.

Tables 1 and 2 illustrate the pixel window size, total time taken for processing, and intensity threshold values used for the canny, Sobel, and averaged intensity difference edge detection algorithms executed on 1060nm SS-OCT and 1310nm SS-OCT 2D images of the human gingival sulcus., The total time taken by edge detection algorithms varies according to the image size. Also, using a trial and error method, the intensity threshold values for the edge detection algorithms was different for each 2D image. This result was due to variations in the thickness of the gingival tissues, and the visibility of the gingival sulcus in OCT images. The averaged values along with the standard deviation of the total time taken to process the images for different intensity threshold values are shown in Tables 1 and 2.

From the values shown in these tables, we can observe that the fastest edge detection algorithm is the Sobel algorithm, but the edge-detected images were lower in sensitivity for identification of the gingival sulcus. The canny edge detection algorithm takes almost three times that of the Sobel edge detection algorithm, but the final images have higher sensitivity for the identification of the gingival sulcus when compared to the Sobel algorithm.

The averaged intensity difference algorithm takes longer to process images in comparison to the canny and Sobel methods. Even though the time taken for processing is higher, the final edge-detected OCT images showed much higher sensitivity for identification of the gingival sulcus in the images. We used two types of pixel window size, 7×7 and 9×7. We observed that the bigger the pixel window size, the longer the processing time for the images, and the clearer the gingival sulcus in the final processed images.

V. CONCLUSIONS

We propose a novel edge-detection algorithm, termed averaged intensity difference for identification of the gingival sulcus in OCT images. The efficiency of our proposed algorithm was compared with conventional edge detection algorithms such as Sobel and canny edge detection. Phantom samples generated using the Microsoft office toolkit were utilized for comparative analysis of all three detection algorithms. 2D OCT images of *in vivo* human gingival sulcus, acquired using 1310nm SS-OCT and 1060nm SS-OCT were used for testing the efficiency of the proposed algorithm and for comparative analysis of the proposed algorithm with the canny and Sobel edge detection algorithms. The Sobel algorithm was highly sensitive to noise and the edges detected for the

gingival sulcus were not continuous or consistent, possibly due to the presence of speckle noise in OCT images. The canny algorithm blurred the OCT images, thereby reducing the noise in the image, but resulting in changing the microstructural details in the OCT image. This, in turn, produced an irregular structure of the detected gingival sulcus. The proposed edge detection algorithm was able to produce images of the gingival sulcus which were clearer and had increased intensity in the OCT images. There were no changes to the microstructures detected in the final processed images. Even though the proposed algorithm has a longer processing time when compared to the canny and Sobel algorithms, it is still fast enough for rapid assessment of OCT images. We believe that the proposed algorithm can be beneficial for researchers and clinical practitioners who use OCT imaging techniques to visualize and assess the gingival sulcus *in vivo* during periodontal diagnosis.

ACKNOWLEDGMENT

(Naresh Kumar Ravichandran and Hoseong Cho contributed equally to this work.)

REFERENCES

[1] P. Dhadse, D. Gattani, and R. Mishra, "The link between periodontal disease and cardiovascular disease: How far we have come in last two decades?" *J. Indian Soc. Periodontology*, vol. 14, no. 3, pp. 148–154, 2010.

[2] I. L. Chapple, R. Genco, and On Behalf of Working Group 2 of the Joint EFP/AAP Workshop, "Diabetes and periodontal diseases: Consensus report of the joint EFP/AAP workshop on periodontitis and systemic diseases," *J. Clin. Periodontology*, vol. 84, no. 40S, pp. S106–S112, 2013.

[3] P. I. Eke, B. Dye, L. Wei, G. Thornton-Evans, and R. Genco, "Prevalence of periodontitis in adults in the United States: 2009 and 2010," *J. Dental Res.*, vol. 91, no. 3, pp. 914–920, 2012.

[4] A. M. Polson, J. G. Caton, R. N. Yeaple, and H. A. Zander, "Histological determination of probe tip penetration into gingival sulcus of humans using an electronic pressure-sensitive probe," *J. Clin. Periodontology*, vol. 7, no. 3, pp. 479–488, 1980.

[5] M. Listgarten, "Periodontal probing: What does it mean?" *J. Clin. Periodontology*, vol. 7, no. 3, pp. 165–176, 1980.

[6] K. Ishihata, N. Wakabayashi, J. Wadachi, T. Akizuki, Y. Izumi, K. Takakuda, and Y. Igarashi, "Reproducibility of probing depth measurement by an experimental periodontal probe incorporating optical fiber sensor," *J. Periodontology*, vol. 83, no. 3, pp. 222–227, 2012.

[7] Research, Science and Therapy Committee, "Position paper: Diagnosis of periodontal diseases," *J. Periodontology*, vol. 74, no. 3, pp. 1237–1247, 2003.

[8] S. Lofthag-Hansen, S. Huumonen, K. Gröndahl, and H.-G. Gröndahl, "Limited cone-beam CT and intraoral radiography for the diagnosis of periapical pathology," *Oral Surg., Oral Med., Oral Pathol., Oral Radiol., Endodontology*, vol. 103, no. 3, pp. 114–119, 2007.

[9] K. Balto, R. Müller, D. Carrington, J. Dobeck, and P. Stashenko, "Quantification of periapical bone destruction in mice by micro-computed tomography," *J. Dental Res.*, vol. 79, no. 3, pp. 35–40, 2000.

[10] D. D. Bosshardt, "The periodontal pocket: Pathogenesis, histopathology and consequences," *Periodontology*, vol. 76, no. 1, pp. 43–50, 2018.

[11] M. Machoy, J. Seeliger, L. Szyszka-Sommerfeld, R. Koprowski, T. Gedrange, and K. Woźniak, "The use of optical coherence tomography in dental diagnostics: A state-of-the-art review," *J. Healthcare Eng.*, vol. 2017, Jul. 2017, Art. no. 7560645.

[12] H. T. Lakshmikantha, N. K. Ravichandran, and H.-S. Park, "Current trends and clinical applications of optical coherence tomography in orthodontics: A literature review," *Dental Med. Problems*, vol. 54, no. 3, pp. 409–415, 2017.

[13] K. Ishibashi, N. Ozawa, J. Tagami, and Y. Sumi, "Swept-source optical coherence tomography as a new tool to evaluate defects of resin-based composite restorations," *J. Dentistry*, vol. 39, no. 8, pp. 543–548, 2011.

[14] M. Segarra, Y. Shimada, A. Sadr, Y. Sumi, and J. Tagami, "Three-dimensional analysis of enamel crack behavior using optical coherence tomography," *J. Dental Res.*, vol. 96, no. 3, pp. 308–314, 2017.

[15] J. B. Eom, J. S. Ahn, J. Eom, and A. Park, "Wide field of view optical coherence tomography for structural and functional diagnoses in dentistry," *J. Biomed. Opt.*, vol. 23, no. 3, 2018, Art. no. 076008.

[16] H. T. Lakshmikantha, N. K. Ravichandran, M. Jeon, J. Kim, and H.-S. Park, "Assessment of cortical bone microdamage following insertion of microimplants using optical coherence tomography: A preliminary study," *J. Zhejiang Univ.-Sci. B*, vol. 19, no. 3, pp. 818–828, 2018.

[17] V. S. M. Carneiro, C. C. B. O. Mota, A. S. L. Gomes, A. F. Souza, N. C. Araújo, R. F. Menezes, and M. E. M. M. Gerbi, "Optical clearing agents associated with nanoparticles for scanning dental structures with optical coherence tomography," in *Proc. Conf. Lasers Electro-Opt. (CLEO)*, San Jose, CA, USA, Oct. 2017, p. JW2A.52.

[18] N. K. Ravichandran, H. T. Lakshmikantha, H.-S. Park, M. Jeon, and J. Kim, "Analysis of enamel loss by prophylaxis and etching treatment in human tooth using optical coherence tomography: An *in vitro* study," *J. Healthcare Eng.*, vol. 2019, Mar. 2019, Art. no. 8973825.

[19] H. T. Lakshmikantha, N. K. Ravichandran, M. Jeon, J. Kim, and H.-S. Park, "3-Dimensional characterization of cortical bone microdamage following placement of orthodontic microimplants using Optical Coherence Tomography," *Sci. Rep.*, vol. 9, Mar. 2019, Art. no. 3242.

[20] L. O. Fernandes, C. C. B. O. Mota, L. S. A. de Melo, M. U. S. da Costa Soares, D. da Silva Feitosa, and A. S. L. Gomes, "*In vivo* assessment of periodontal structures and measurement of gingival sulcus with optical coherence tomography: A pilot study," *J. Biophoton.*, vol. 10, nos. 6–7, pp. 862–869, 2017.

[21] C. C. B. O. Mota, L. O. Fernandes, R. Cimões, and A. S. L. Gomes, "Non-invasive periodontal probing through Fourier-domain optical coherence tomography," *J. Periodontology*, vol. 86, no. 3, pp. 1087–1094, 2015.

[22] S. Kakizaki, A. Aoki, M. Tsubokawa, T. Lin, K. Mizutani, G. Koshy, A. Sadr, S. Oda, Y. Sumi, and Y. Izumi, "Observation and determination of periodontal tissue profile using optical coherence tomography," *J. Periodontal Res.*, vol. 53, no. 2, pp. 188–199, 2018.

[23] S.-R. Kang, J.-M. Kim, S.-H. Kim, H.-J. Park, T.-I. Kim, and W.-J. Yi, "Tooth cracks detection and gingival sulcus depth measurement using optical coherence tomography," in *Proc. IEEE 39th Annu. Int. Conf. Eng. Med. Biol. Soc. (EMBC)*, Jul. 2017, pp. 4403–4406.

[24] S.-H. Kim, S.-R. Kang, H.-J. Park, J.-M. Kim, W.-J. Yi, and T.-I. Kim, "Improved accuracy in periodontal pocket depth measurement using optical coherence tomography," *J. Periodontal Implant Sci.*, vol. 47, no. 1, pp. 13–19, 2017.

[25] S.-C. Chang, H.-Y. Syu, Y.-L. Wang, C.-J. Lai, S.-Y. Huang, and H.-C. Wang, "Identifying the incidence level of periodontal disease through hyperspectral imaging," *Opt. Quantum Electron.*, vol. 50, no. 3, p. 409, 2018.

[26] N. M. Le, S. Song, H. Zhou, J. Xu, Y. Li, C.-E. Sung, A. Sadr, K.-H. Chung, H. M. Subhash, and L. Kilpatrick, "A noninvasive imaging and measurement using optical coherence tomography angiography for the assessment of gingiva: An *in vivo* study," *J. Biophoton.*, vol. 11, no. 12, 2018, Art. no. e201800242.

[27] D. Lee, C. Lee, S. Kim, Q. Zhou, J. Kim, and C. Kim, "*In vivo* near infrared virtual intraoperative surgical photoacoustic optical coherence tomography," *Sci. Rep.*, vol. 6, Oct. 2016, Art. no. 35176.

[28] J. Rogowska and M. E. Brezinski, "Image processing techniques for noise removal, enhancement and segmentation of cartilage OCT images," *Phys. Med. Biol.*, vol. 47, no. 3, p. 641, 2002.

NARESH KUMAR RAVICHANDRAN received the B.E. degree in electronics and communication engineering from St. Peter's University, Chennai, India, and the M.Sc. degree in electronics engineering from Kyungpook National University, Daegu, South Korea, where he has been a Ph.D. Researcher with the Electronics Engineering Department, since 2016. His research interests are in the developing and optimizing novel biological imaging techniques with possible applications in dental, agronomical studies, entomological studies, and industrial applications.

HOSEONG CHO is currently pursuing the B.Sc. degree in electronics engineering with Kyungpook National University, Daegu, South Korea. His research interests are in image processing and analysis biomedical imaging techniques.

JAEYUL LEE is currently pursuing the Ph.D. degree with the School of Electronics Engineering, Kyungpook National University, Daegu, South Korea. His research interests include optical imaging techniques, photoacoustic microscopy, optical coherence tomography, and handheld instruments for optimization of the optical coherence tomography and photoacoustic microscopy systems.

SANGYEOB HAN is currently pursuing the Ph.D. degree with the School of Electronics Engineering, Kyungpook National University, Daegu, South Korea. His research interests include optical imaging techniques, photoacoustic microscopy, optical coherence tomography, and multiphoton microscopy.

RUCHIRE ERANGA WIJESINGHE received the B.Sc. and Ph.D. degrees in electronics engineering from Kyungpook National University, Daegu, South Korea, in 2012 and 2018, respectively. He is currently an Assistant Professor with the Department of Biomedical Engineering, Kyungil University. His research interests are in the development of high-resolution novel biological and biomedical imaging techniques, including optical coherence tomography and microscopy for clinical utility.

PILUN KIM received the Ph.D. degree from the Department of Medical and Biological Engineering, Kyungpook National University, in 2011, where he is currently a Researching Visiting Professor with the Institute of Biomedical Engineering. He is interested in translating new technologies from the research field to the application field, such as clinic and industrial and making its productization. His main research interests include biomedical device development, optical coherence tomography (oct), and digital image processing.

JAE-WON SONG received the Ph.D. degree in electrical and electronics engineering from the Korea Advanced Institute of Science and Technology, Daejeon, South Korea, in 1984. He is currently a Professor with the School of Electronics Engineering, Kyungpook National University. His research interests are in the development of optical communication and integrated optics.

MANSIK JEON received the Ph.D. degree in electronics engineering from Kyungpook National University, Daegu, South Korea, in 2011, where he is currently an Assistant Professor with the School of Electronics Engineering. His research interests are in the development of nonionizing and noninvasive novel biomedical imaging techniques, including photoacoustic tomography, photoacoustic microscopy, optical coherence tomography, ultrasonic imaging, handheld scanner, and their clinical applications.

JEEHYUN KIM received the Ph.D. degree in biomedical engineering from The University of Texas at Austin, Austin, TX, USA, in 2004. He was a Postdoctoral Researcher with the Beckman Laser Institute, University of California at Irvine. He is currently a Full Professor with Kyungpook National University, Daegu, South Korea. His research interests are in biomedical imaging and sensing, neuroscience studies using multiphoton microscopy, photo-acoustic imaging, and other novel applications of sensors.